Discrimination of dynamically and post-dynamically recrystallized grains based on EBSD data. Application to Inconel 718

Alexis Nicolaÿ, Jean-Michel Franchet, Jonathan Cormier, Haithem Mansour, Marc de Graef, Anthony Seret, Nathalie Bozzolo

Discrimination of dynamically and post-dynamically recrystallized grains based on EBSD data. Application to Inconel 718

A. Nicolaÿ[1,2*], J.M. Franchet[2], J. Cormier[3], H. Mansour[4], M. De Graef[5], A. Seret[1], N. Bozzolo[1]

[1] MINES ParisTech, PSL – Research University, CEMEF – Centre de mise en forme des matériaux, CNRS UMR 7635, CS 10207 rue Claude Daunesse, 06904 Sophia-Antipolis cedex, France
[2] Safran SA, SafranTech – Materials & Process Department, rue des Jeunes Bois – Châteaufort – CS 80112 78772, Magny-Les-Hameaux Cedex, France
[3] Institut Pprime, Physics and Mechanics of Materials Department, UPR CNRS 3346, ISAE-ENSMA, 1 avenue Clément Ader, BP 40109, 86961 Futuroscope, Chasseneuil, France
[4] Oxford Instruments NanoAnalysis, 77 ZA de Montvoisin, Gômetz-la-Ville, France
[5] Carnegie Mellon University – Department of Materials Science and Engineering 5000 Forbes Ave. Pittsburgh, Pennsylvania 15213, USA
* Correspondence: alexis.nicolay@mines-paristech.fr / +33 493 95 75 55
Key words: EBSD, angular resolution, recrystallization, ECCI

Abstract

The importance of angular resolution in EBSD analyses is discussed based on an Inconel 718 sample containing several populations of recrystallized grains, with subtle differences in dislocation contents. Classical EBSD analyses (with angular resolution in the range of 0.5-1°) do not allow for distinguishing recrystallized grains grown dynamically or post-dynamically. The angular resolution of EBSD orientation and misorientation data can be significantly improved (down to about 0.1-0.2°) either using more sophisticated Kikuchi pattern indexing methods and/or using the recently proposed LLASS denoising filter (Local Linear Automatic Smoothing Splines). Then the co-existence of both dynamically and post-dynamically recrystallized grains in the sample can be confirmed and quantified. ECCI images unambiguously confirm the conclusions drawn from the analysis of improved angular resolution EBSD data, and furthermore reveal the presence of thermal stress induced dislocations with typical patterns in water quenched Inconel 718 recrystallized grains.

Introduction

Polycrystalline nickel-based superalloys are widely used in the hottest parts of aircraft engines due to their good mechanical properties at high temperature. These parts are generally obtained by hot-forging. Since it represents approximately one third of the weight of current aircraft engines, Inconel 718 is one of the most important Nickel-based superalloys (Texier et al. 2016).

Generally, low to medium stacking fault energy (γ_{SFE}) alloys undergo recrystallization during hot forging operations (Humphreys & Hatherly, M., 2017; Sakai et al., 2014). Inconel 718 and the other Nickel-based superalloys are among such alloys (Azarbarmas et al., 2016; Wang et al., 2008; Zhao et al. 1994).

Depending on thermomechanical conditions (temperature, strain level and strain rate), recrystallization can occur dynamically during deformation and/or post-dynamically as massive industrial pieces cannot be cooled down instantaneously. As a consequence, dynamic recrystallization (DRX) referring to recrystallization that occurs during deformation must be

distinguished from post-dynamic recrystallization (PDRX) referring to recrystallization that occurs after deformation. Within the post-dynamic regime, meta-dynamic recrystallization (MDRX) and/or static recrystallization (SRX) are two different recrystallization mechanisms which can occur and contribute to the PDRX. The MDRX strictly consists in the growth of DRX grain nuclei under the influence of the difference in stored energy between the recrystallized grains and the surrounding deformed matrix. Here the MDRX definition will be extended to the growth of DRX grains and not only DRX grain nuclei. The SRX consists in both nucleation and growth of new grains after deformation stopped.

Because recrystallized and non-recrystallized grains have different dislocation densities and therefore different intragranular misorientation levels, they can be quite easily distinguished by means of standard EBSD analyses, with angular resolution classically of the order of 0.5° (Maitland & Sitzman, S., 2007), using parameters quantifying local misorientations (Poelt et al., 2006; Zouari et al., 2017; Zouari et al., 2016). Contrary to PDRX grains which appear and grow after deformation, DRX grains appear and grow during deformation. As a consequence, DRX grains are theoretically more strain hardened than PDRX grains owing to their formation mechanisms, even if the difference in dislocation density remains lower compared to the difference in dislocation density between these respective recrystallized grains families (DRX and PDRX) and non-recrystallized grains.

PDRX can hardly be avoided under industrial conditions because of the slow cooling rates inherent to massive pieces. The final microstructure of a forged component thus depends on both DRX and PDRX kinetics. Deriving predictive models requires identification of the kinetics of both regimes for given forging conditions (temperature, strain rate, and strain level). It is thus necessary to distinguish between both populations, which is usually not possible using standard EBSD data analyses as shown below.

As a consequence, EBSD data with improved angular resolution could have an interest for such applications. Three different approaches will be tested below, and a direct observation of dislocations using electron channeling contrast imaging (ECCI) will serve to validate the results obtained from the EBSD based approaches.

1. Material and Procedure

A compression test was performed on a cylindrical specimen ($\phi 10mm \times 15mm$) taken at mid-radius of a $200mm$ diameter billet of Inconel 718 whose composition is given in **table 1**.

Elements	Ni	Cr	Mo	Nb	Al	Ti	Fe
% weight	Bal.	17.9	2.9	5.4	0.5	1.0	18.3

Table 1 *- Chemical composition of Inconel 718 billet used in this work*

Before compression, the sample is heated at 5°C.s^{-1} and then maintained at the deformation temperature chosen below the δ solvus temperature ($T = 980\ °C$) for 5 minutes. The microstructure obtained after such holding and water quenching is shown on **Figure 1a, 1b, and 1c.** In the following, it will be referred to as the "initial microstructure" for discussing the changes occurring during and after hot-deformation. The initial grain size (defined as the mean equivalent circle diameter of the grains detected based on a 10° misorientation angle threshold and ignoring twin boundaries) is $\overline{\emptyset_{eq}} \approx 18\mu m$. The initial δ phase volume fraction was estimated at $f_\delta \approx 0.2\%$ after grey level thresholding of backscattered electron images. Thermomechanical parameters for the compression test are chosen in order to produce a partially dynamically recrystallized microstructure (Wang et al., 2008; Zhao et al. 1994). The specimen was actually deformed on a Gleeble 3800 at $T = 980\ °C$ and $\dot{\varepsilon} = 0.01\ s^{-1}$ up to a macroscopic strain $\varepsilon = 0.7$. After compression, the specimen was held for more than 5s to leave time for post-dynamic evolutions to occur, and then water quenched. The PDRX kinetics are indeed known to be very fast, and 5s holding time after deformation should be enough to get a significant evolution (Na et al., 2003; Zouari et al., 2017). Following this procedure, the final microstructure should thus encompass both DRX and PDRX grains.

The specimen was then cut through an in-diameter longitudinal direction of the cylinder for metallographic preparation and was analysed at the centre where the local equivalent strain reaches $\bar{\varepsilon} \approx 1.2$ for the applied macroscopic strain $\varepsilon = 0.7$. To achieve a surface quality suitable for EBSD analyses, the surface was first pre-polished using SiC abrasive papers (down to a SiC granulometry of 5µm), then mechanically polished using 3µm and 1µm diamond suspension solution, and finally electropolished for 5 seconds with a solution of 10% perchloric acid in ethanol at -5°C.

The EBSD data analysed in this paper were all acquired on the same sample area but using three different systems:

i. A Carl Zeiss Supra 40 field emission gun scanning electron microscope (FEGSEM) equipped with a Bruker Quantax system comprising EBSD e$^-$Flash^{HR} detector and the Esprit 2.1 software package. The Bruker system uses the Hough transform to detect Kikuchi bands in the EBSD patterns, and then indexes the patterns with the highest possible number of bands, starting from 12, based on the angle between those bands. Such Hough-transform and band-angles based approach is rather classical and used in most commercial systems, with variations in the strategies implemented into the indexing algorithm. The high number of bands used in the Bruker algorithm provides very few misindexings and a low rate of non-indexed points (typically less than 1% for the material under study).
ii. A Carl Zeiss Supra 55 FEGSEM equipped with a Symmetry EBSD detector and AZtec software package from the Oxford company. The Oxford Symmetry system is a new generation detector with a CMOS instead of a CCD sensor, and provides

higher sensitivity as compared to former technologies (Mansour et al., 2017). Furthermore, the patterns acquired with the Symmetry detector were indexed using a different algorithm, providing a higher orientation measurement precision. After primary band detection performed using an optimized variant of the classical Hough transform approach (it picks out peaks with sub-pixel resolution in Hough space), the pattern is indexed with a user-defined number of bands (typically at least 7 or 8 bands; up to 11 or 12), which leads to a first crystal orientation estimate. At this stage, orientation is thus determined classically and with a precision in the range of 0.2-0.5°. Then an additional step ("Refined Accuracy") is performed to refine the solution: the initial proposed solution is used to model, under kinematical assumptions, the expected positions of the Kikuchi band edges using Bragg's theory, taking into account their hyperbolic nature. Detailed image analysis along the band edges in the original diffraction pattern then enables a refinement of the original solution, maximizing the fit between the solution and the original pattern (see US patent No. 9,671,354 B2 (2017) for further details). The angular resolution of EBSD analyses can thus routinely be improved down to 0.05°, or even better with high pattern quality.

iii. The patterns produced with the Bruker system mounted onto the Zeiss Supra 40 microscope were stored and re-analysed using the dictionary indexing method described in (Chen et al., 2015). In this approach, a physics-based model is used to compute dynamical scattering intensities in the form of a master Kikuchi pattern (Callahan & De Graef, 2013) from which individual patterns are extracted by means of bilinear interpolation. The simulation takes into account the energy distribution of the back-scattered electrons over the surface of the detector, as well as the depth distribution in the sample. Patterns are simulated for a set of orientations uniformly sampling orientation space (Singh & De Graef, 2016), and the resulting dictionary of patterns is then used to determine the most likely orientation for each experimental pattern using a pattern similarity metric, in this case the dot product between normalized patterns. The best matching orientation is then further refined using a bound optimization by quadratic approximation (BOBYQA) approach (Powell, 2009), which typically results in orientation determinations with an accuracy of around 0.05° for noise-free patterns.

Maps of 200x150 points were acquired on the same sample area and a constant step size of 0.2 µm using these three EBSD systems, with 99.8%, 98.7%, and 100% of hit rate respectively. In the following, data provided by the first EBSD acquisition system (i) will be labelled as "conventional", data provided by the second one (ii) will be labelled as "improved angular resolution method", and data provided by the third one (iii) will be labelled as the "whole pattern indexing method".

All three data sets were furthermore filtered using a newly developed filter (Seret et al., under revision), that is able to reduce the orientation noise preserving dislocations substructures and will be referred to as LLASS filter in the following (Local Linear Automatic Smoothing Splines). This filter is applied to raw orientation data using the MTEX toolbox (Bachmann et al., 2011) within the Matlab environment. The principle of this filter derives from the smoothing splines method with an automatic calibration made possible by rewriting the classical smoothing term. Raw and filtered EBSD data are then analysed in view of differentiating DRX and PDRX grains. From this perspective, two misorientation parameters are used since they vary with the dislocation density (Moussa et al., 2015; Seret et al., submitted); the Kernel Average Misorientation (KAM) that is a local property (one value per measuring point) and the Grain Average KAM (GAKAM) that is a grain property (one

value per grain). The KAM value of a given point is equal to the average of the misorientation angles θ_{ij} between this point i and its n neighbours j (**equation 1**). The GAKAM value of a grain k which is used in the present work is the average value of misorientation angles between all pairs of neighbouring points in this grain. In other words, it is equivalent to the average of the KAM values of all points of the grain (**equation 2**).

$$KAM_i = \frac{1}{n}\sum_{j=1}^{n}\theta_{ij} \quad (1)$$

$$GAKAM_k = \frac{1}{N}\sum_{k=1}^{N}\frac{1}{n}\sum_{j=1}^{n}\theta_{ij} \quad (2)$$

Since analysing intragranular misorientations is an indirect method for revealing the presence of dislocations and estimating their density, ECCI was also performed to confirm the presence/absence of dislocations in given grains. It is worth mentioning here that ECCI was not performed in a well-controlled manner as introduced by Zaefferer and al. (Zaefferer et al., 2014), but simply by checking the contrasts under different tilt angles around the initial position. In their work, based on the interpretation of electrons channelling by Bloch waves theory as proposed earlier by Hirsh and al. (Hirsh et al., 1965) and reviewed in (Schulson et al., 1977), Zaefferer and al. show that there are optimal conditions (so-called "two-beam diffraction conditions") for electron channelling and enhancing crystalline defect contrasts, depending on the local orientation in relation to the electron beam direction. In the present study, such a rigorous approach, i.e. controlling channelling conditions, would be tedious at the scale of the studied polycrystalline microstructure. On the one hand, this would imply an optimal ECCI condition for each grain, and on the other hand the potential misorientation in a given grain leads to different optimal ECCI conditions inside this grain. Being off optimal contrast conditions does not prevent from visualizing dislocations, except for very specific crystal orientations.

Indeed, as has been confirmed several times in the literature (Crimp et al., 2001, Crimp et al., 2006; Mansour et al., 2014), imaging of a given dislocation in ECCI also obeys the well-known TEM invisibility criteria $\boldsymbol{g}\cdot\boldsymbol{b}=\boldsymbol{0}$ (screw, edge, and mixed dislocations) and $\boldsymbol{g}\cdot\boldsymbol{b}\times\boldsymbol{u}=\boldsymbol{0}$ (edge and mixed dislocations), where g is the active diffraction vector for a crystallographic plane (hkl), b the Burgers vector, and u the dislocation line direction.

To determine whether a grain contains dislocations or not, several backscattered electron images were recorded at different tilt angles (varying by a few degrees around the initial position). There is very little chance that all dislocations in a given grain could be in their strict extinction conditions for the whole tilt series. It will be concluded that there is no dislocation in a given area if none of the images exhibit dislocation contrast.

2. Results and discussion

The initial microstructure is fully recrystallized and has rather large equiaxed grains ($\overline{\emptyset_{eq}} \approx 18\mu m$, number average equivalent circle diameter calculated after detecting grains with a 10° threshold and ignoring twin boundaries) as shown on **Figures 1a, 1c and 1e**. After deformation, the grain size has been significantly refined by recrystallization (**Figures 1b and 1d**), and few unrecrystallized areas remain.

Thanks to this first standard EBSD analysis of the deformed microstructure over a quite large area, recrystallized and non- recrystallized grains can be quite easily identified via the GAKAM parameter coupled with a grain size criterion given that recrystallization leads to grain refinement (see **Figure 1**). The corresponding non-recrystallized grains are identified (marked by thicker grain boundaries and red arrows) on **Figure 1d** after setting GAKAM and grain size threshold to 0.65° and 15µm respectively.

The red frame on KAM map of **Figure 1d** delimits an area of interest for the next analyses since it contains only recrystallized grains.

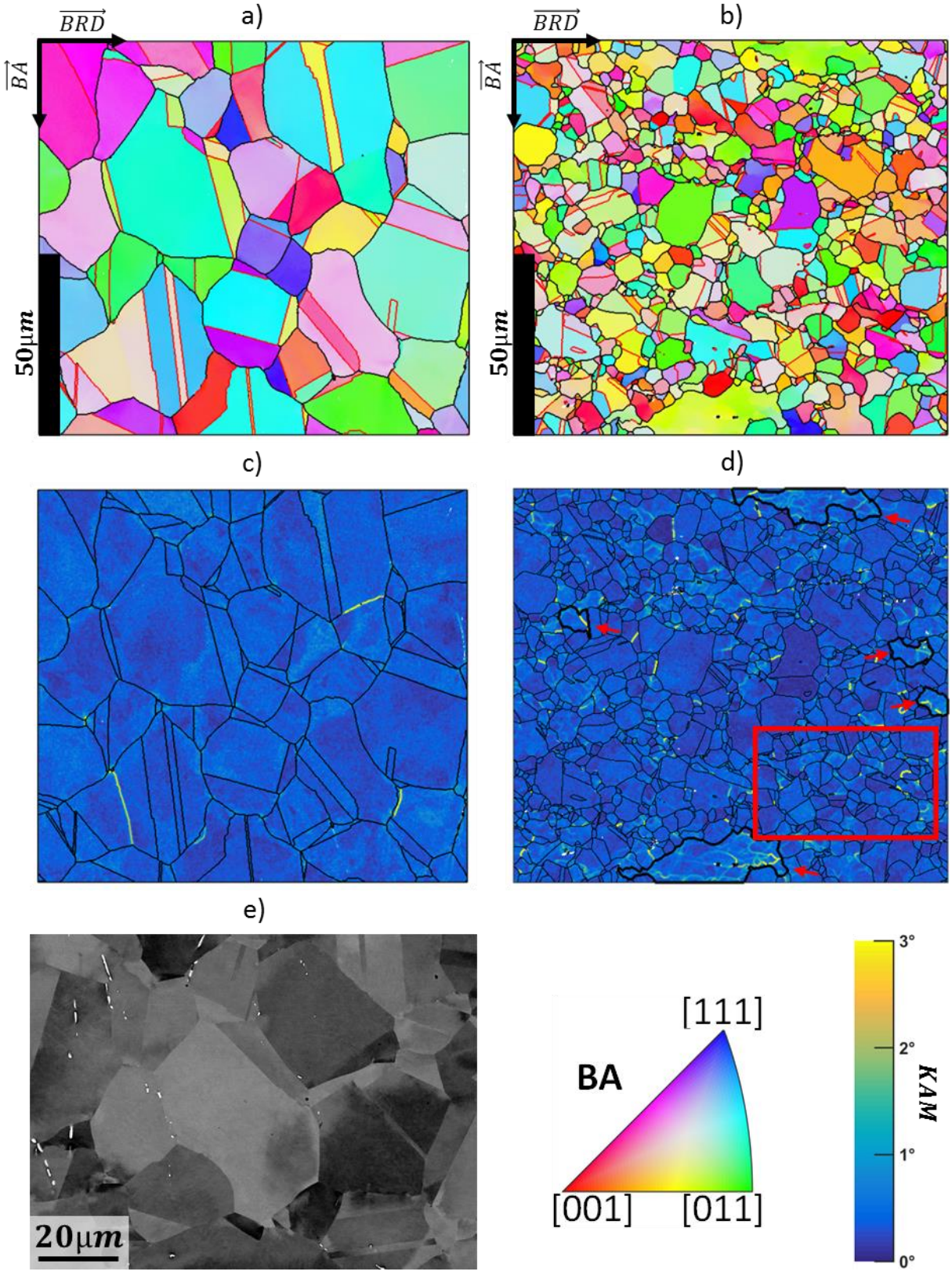

***Figure 1**: The microstructure just before compression (initial microstructure) is presented on a) Orientation map obtained by conventional EBSD mapping with 99% indexing (the Bilet Axis direction BA and the Bilet Radius Direction BRD are indicated). Grain boundaries (>10°) are plotted black and twin boundaries red, c) Corresponding KAM map, and e) Backscattered electron image highlighting δ phase in white. The deformed microstructure at center is presented on b) Orientations map which can be directly compared to **figure 1a** since the scales are equivalent and e) Corresponding KAM map on which the red rectangle highlights the area that will be studied into details in the following.*

2.1. DRX and PDRX populations: qualitative approach

Figure 2 shows KAM maps and corresponding KAM distributions obtained from different EBSD data sets of the same area containing only recrystallized grains and highlighted on **Figure 1d**. Maps presented on **Figure 2a, 2c and 2e** correspond to the raw data obtained with the conventional method, the improved angular resolution method, and the whole pattern indexing method, respectively. KAM maps of **Figure 2b, 2d and 2f** correspond respectively to the same data as in **Figure 2a, 2c and 2e** but after reduction of the measurement noise by means of the LLASS filter.

The progressive decrease in orientation noise from **Figure 2b to 2f** makes it possible to qualitatively highlight two types of recrystallized grains based on their intragranular misorientation levels (i.e., dislocation contents), which may correspond to DRX and PDRX grains populations. Given the DRX and PDRX grain definition, grains with higher and more heterogeneous KAM values could be considered as DRX grains (grains 1 and 2 on **Figure 2d**) while grains having lower and more homogeneous KAM values could be considered as PDRX grains (grains 3 and 4 on **Figure 2d**).

Distinguishing both populations with confidence is definitely not possible using only the conventional data set seen in **Figure 2a,** due to the standard measurement noise (here about 0.4°). It is actually possible to identify the two populations of recrystallized grains on this figure only once the results with lower orientation noise have been shown. The LLASS filter applied to the conventional raw data set qualitatively leads to results that are very similar to raw data set with improved angular resolution method. That same filter applied onto the improved angular resolution method raw data set still allows for a slight increase in precision, as the low KAM value end of the distribution shifts slightly to the left.

The raw data from the improved whole pattern indexing method is similar to that obtained after applying the LLASS filter on the data from the improved angular resolution method. On the one hand, it can be noticed that indexing EBSD data based on dynamic simulations (whole pattern indexing method) leads to a better angular precision than indexing EBSD data based on kinematic simulation (improved angular resolution method), although the latter indexing method already improves significantly the angular resolution compared to conventional EBSD data. On the other hand, these results confirm once again that the LLASS filter is quite efficient in reducing noise measurement and has the great advantage over the other method that it can be used with conventional EBSD system and data. Application of the LLASS filter to the whole pattern indexing raw data does not change anything in the KAM map and the corresponding distribution.

a)

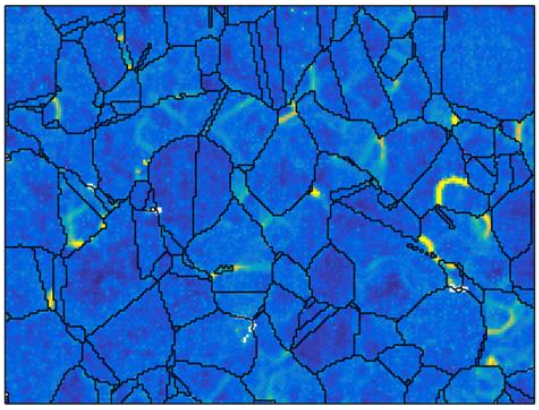

g)

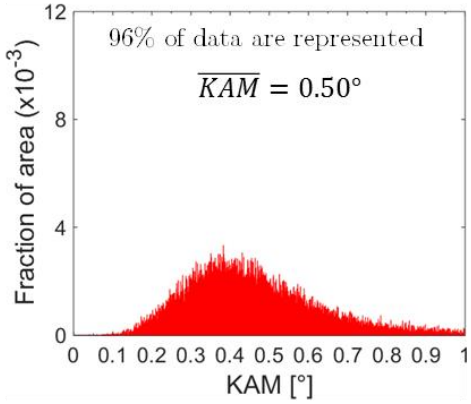
96% of data are represented
$\overline{KAM} = 0.50°$
Fraction of area (x10^{-3})
KAM [°]

b)

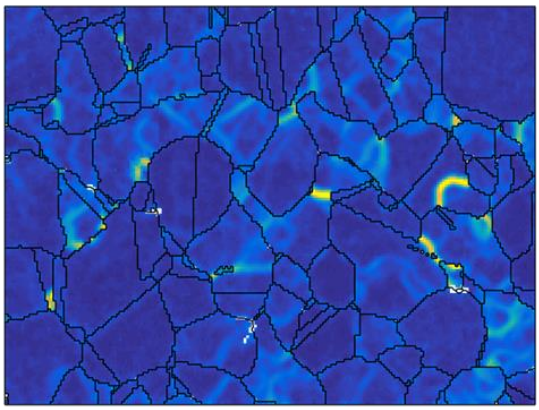

h)

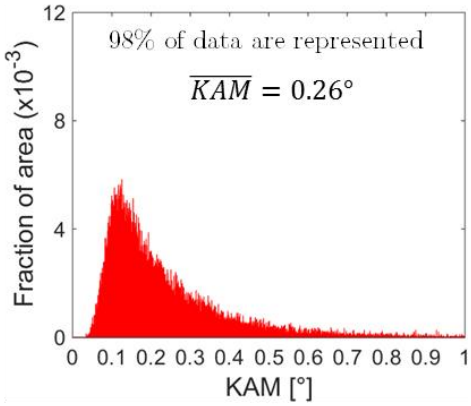
98% of data are represented
$\overline{KAM} = 0.26°$
Fraction of area (x10^{-3})
KAM [°]

c)

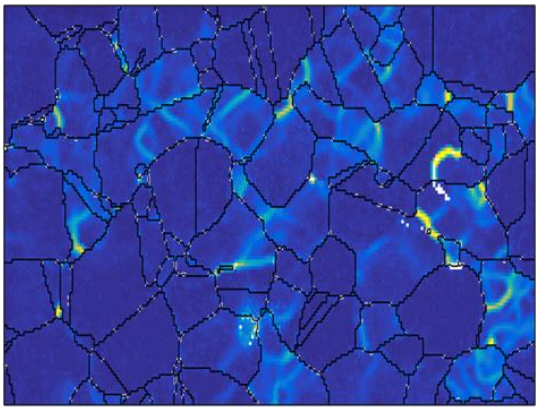

i)

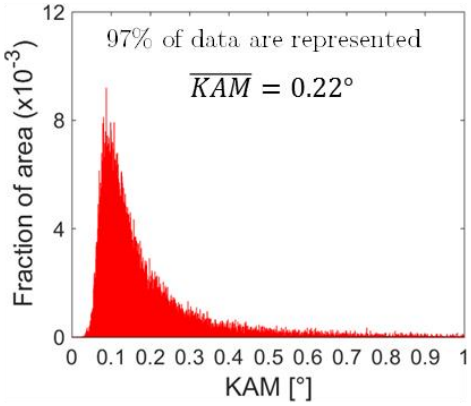
97% of data are represented
$\overline{KAM} = 0.22°$
Fraction of area (x10^{-3})
KAM [°]

d)

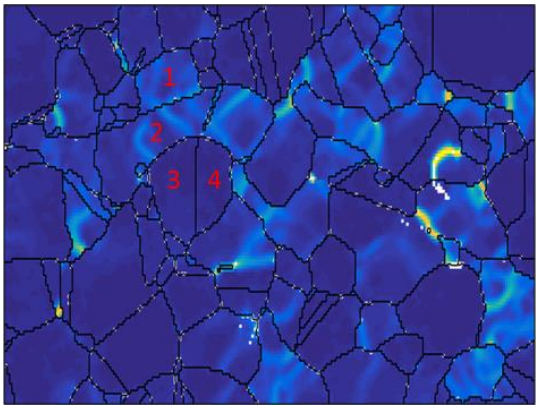
1
2
3
4

j)

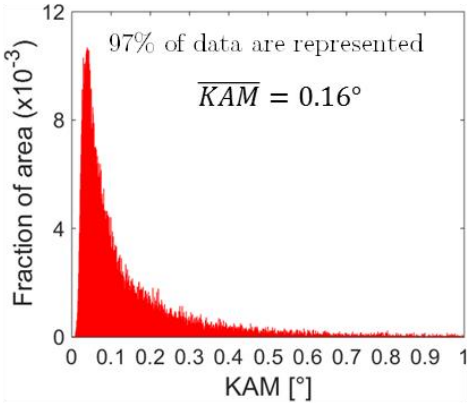
97% of data are represented
$\overline{KAM} = 0.16°$
Fraction of area (x10^{-3})
KAM [°]

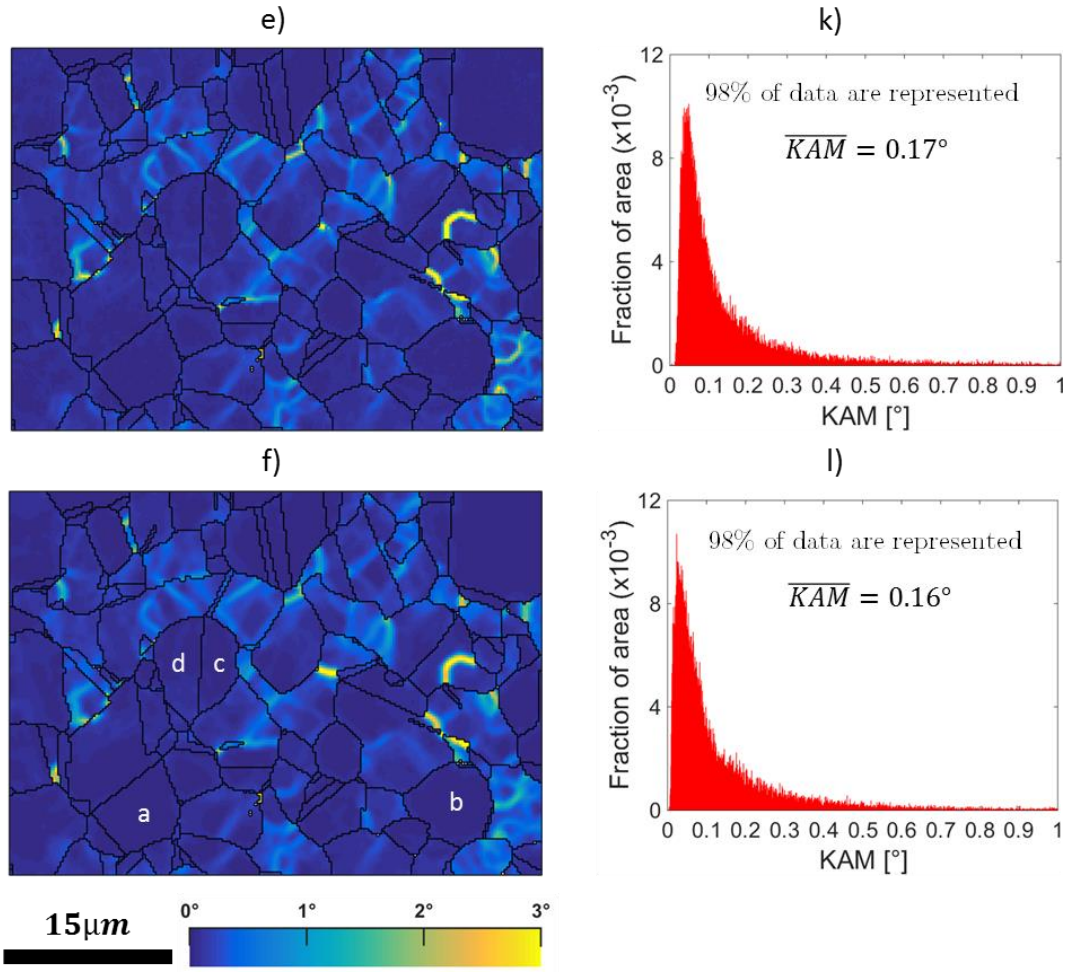

Figure 2*: KAM map and distribution for a),g) raw EBSD data acquired with standard angular resolution, b),h) LLASS-filtered EBSD data acquired with standard angular resolution c),i) raw EBSD data acquired with the improved angular resolution method d),j) LLASS-filtered EBSD data acquired with the improved angular resolution method, e),k) raw EBSD data acquired with the whole pattern indexing method f),l) LLASS-filtered EBSD data acquired with the whole pattern indexing method*

In order to definitely confirm that the two populations of recrystallized grains with low and high KAM / dislocation content really correspond to DRX and PDRX grains, ECCI images have been acquired on an area which was also characterized by conventional angular resolution EBSD whose resulting data was filtered using the LLASS filter. This area is not the same as the one used for the previous comparisons of EBSD acquisitions and post-processing because carbon contamination of the area submitted to several successive EBSD scans prevented the acquisition of suitable ECCI micrographs. Although better results can be obtained with the improved angular resolution and the whole pattern indexing methods (with or without filtering data), as shown previously in **Figure 2,** the LLASS filter applied onto conventional EBSD data allows to identify the two same populations of recrystallized grains. Nowadays, conventional EBSD analysis still remains the most common approach, this is one reason why the orientation maps obtained after filtering conventional EBSD data will be used in the following comparison with ECCI images. Using any of the presented methods leading to low noise orientation data for those comparisons would anyway lead to the same conclusions.

Grains numbered from 1 to 5 on **Figure 3d** have been identified as PDRX grains after EBSD analysis (**Figure 3a**). ECCI images of these grains and surrounding DRX grains shown in **Figure 3 b-f** lead to the same conclusions regarding dislocation density in these two

populations of recrystallized grains. Dislocation density in DRX grains is qualitatively higher than in PDRX grains. Furthermore, it can be observed that dislocation highlighting in DRX grains is not sensitive to the tilt angle as some dislocations remain visible for all tilt angles, as a result of the orientation gradient induced in those grains by the dislocations themselves. A DRX grain cannot be in a uniform condition with regards to the electron channeling process. In PDRX grains, the backscattered electron intensity remains very homogeneous at each tilt angle, consistent with their uniform orientation. Only a few dislocations can be seen at the given tilt angles (in **Figure 3,** individual dislocations near yellow arrows in grain 1 at a tilt angle of -1°, and in grain 5 at a tilt angle of -1° and 2°. A region in grain 3 near blue narrow at a tilt angle of -2° and 1°, and grain 5 at a tilt angle of -1° and 2°); these may be due to the fact that the sample has been water quenched at the end of the experiment, as demonstrated below.

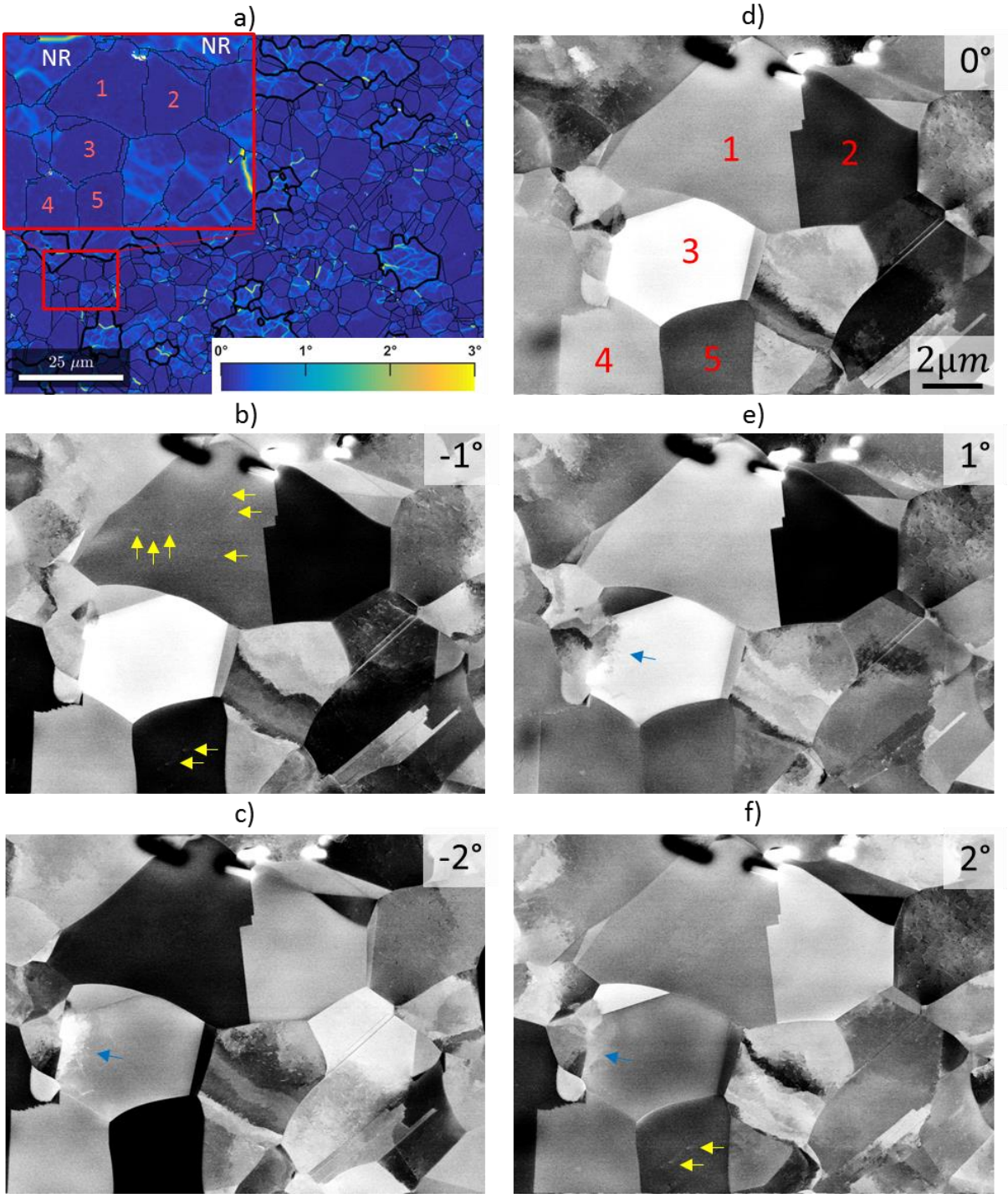

***Figure 3**: a) KAM map obtained with data coming from conventional angular resolution EBSD acquisition filtered with the LLASS denoising filter. NR area corresponds to parts of unrecrystallized grains. b), c), d),e), and f) are ECCI images at different tilt angles around the initial position (indicated on each picture) of an area containing both DRX and PDRX grains identified on a).*

Two other samples of the same material were deformed at room temperature and then annealed to be statically recrystallized. After annealing, one was water quenched and the other one was slow cooled, so that the possible effect of water quenching could be assessed. ECCI micrographs of statically recrystallized grains either quenched (right column) or slow cooled (left column) are shown in **Figure 4**. KAM maps and distribution histograms obtained from

data coming from filtered conventional EBSD analyses performed on SRX grains samples used for **Figure 4** are plotted in **Figure 5**.

While no dislocation can be seen in slow cooled SRX grains (**Figure 4 a-d**), some dislocations appear in water quenched SRX grains (**Figure 4 e-g**). KAM values in water quenched and slow cooled SRX grains are similar leading to close KAM distributions (**Figure 5)**. From **Figure 4** and **5**, it can thus be concluded that, as a result of plastic flow under thermal stresses, water quenching obviously introduces dislocations in the recrystallized grains but without any measurable impact on misorientations in filtered conventional EBSD data.

In addition, it can be noted that the dislocation configurations resulting from plastic deformation during quenching and resulting from hot deformation in DRX grains are quite different. On the one hand, dislocation repartitions in DRX grains do not seem to follow any special pattern. On the other hand, in some water quenched SRX grains (for example grains A, B, C and D on **Figure 4**), and for tilt conditions that render dislocations visible by ECCI, the visible dislocations are aligned.

The few dislocations revealed by ECCI in PDRX grains on **Figure 3** could thus result from quenching; for example, the dislocations in grain 5 are aligned (see **Figure 3** for tilt angle of -1° and 2°) and describe a pattern similar to that of water quenched SRX grains of the right column of Figure 4. Another possible explanation for the presence of dislocations in PDRX grains could be that these grains are actually metadynamically recrystallized grains (DRX grains which kept growing during holding after deformation). It seems to be the case for grain number 3 of **Figure 3,** given that a part of it has some DRX characteristics and the other part has PDRX characteristics. Indeed, the left side of grain 3 exhibits contrast due to orientation variations and high unstructured dislocation density that is weakly sensible to tilt angle. In addition, dislocations revealed on the left side of this grain have an impact on the measured local misorientations (see **Figure 3a**). This means that dislocations in this left area do not originate only from quenching thermal stresses, but also from hot deformation.

Even if, among PDRX grains identified in **Figure 3,** grain 3 is likely to be a MDRX grain since it has the corresponding characteristics (in ECCI and in EBSD), it would not be true to consider the other PDRX grains as SRX grains. The PDRX grains that do not exhibit a DRX area in the observed 2D section, could have one out of that surface, as schematized on **Figure 6**. On this figure, a MDRX grain is considered. The section plane A (see **Figure 6b**) is within the area/volume that has been swept by the recrystallization front during the post-dynamic holding. This section of the grain does not contain any dislocations (or only those which would be induced by water quenching). The section plane B (see **Figure 6c**) runs through the original small PDRX grain that led to the large MDRX grain, and thus includes an area with dislocations and misorientations typical for DRX grains. In other words, a PDRX grain seen in a A type section (e.g. grains 1,2,4, or 5 on **Figure 3**) cannot be identified as SRX or MDRX grains whereas a PDRX grain seen in B type section (e.g. grain 3 on **Figure 3**) can be identified as MDRX grain. Performing serial FIB sectioning and 3D EBSD characterization could be a good alternative to solve this problem and should make it possible to distinguish MDRX and SRX grains at least qualitatively provided that the EBSD measurement noise remains low enough.

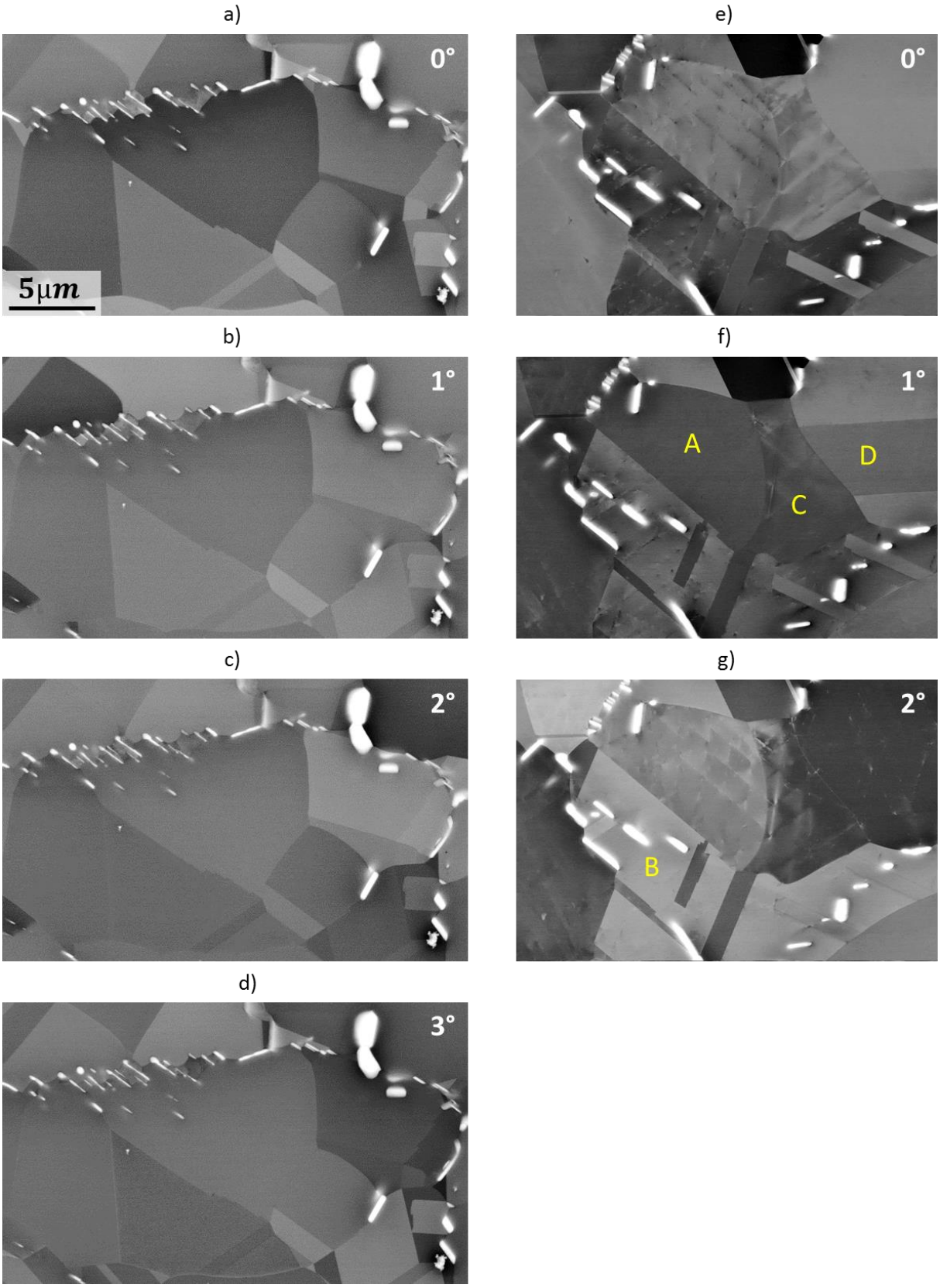

***Figure 4**: ECCI micrographs of SRX grains produced by a cold deformation of Inconel 718 followed by a thermal treatment. On the left column from a) to d), the sample has been slowly furnace-cooled down to room temperature. On the right column from e) to g), the sample has been water quenched at the end of the thermal treatment. White particles are δ-Ni_3Nb precipitates.*

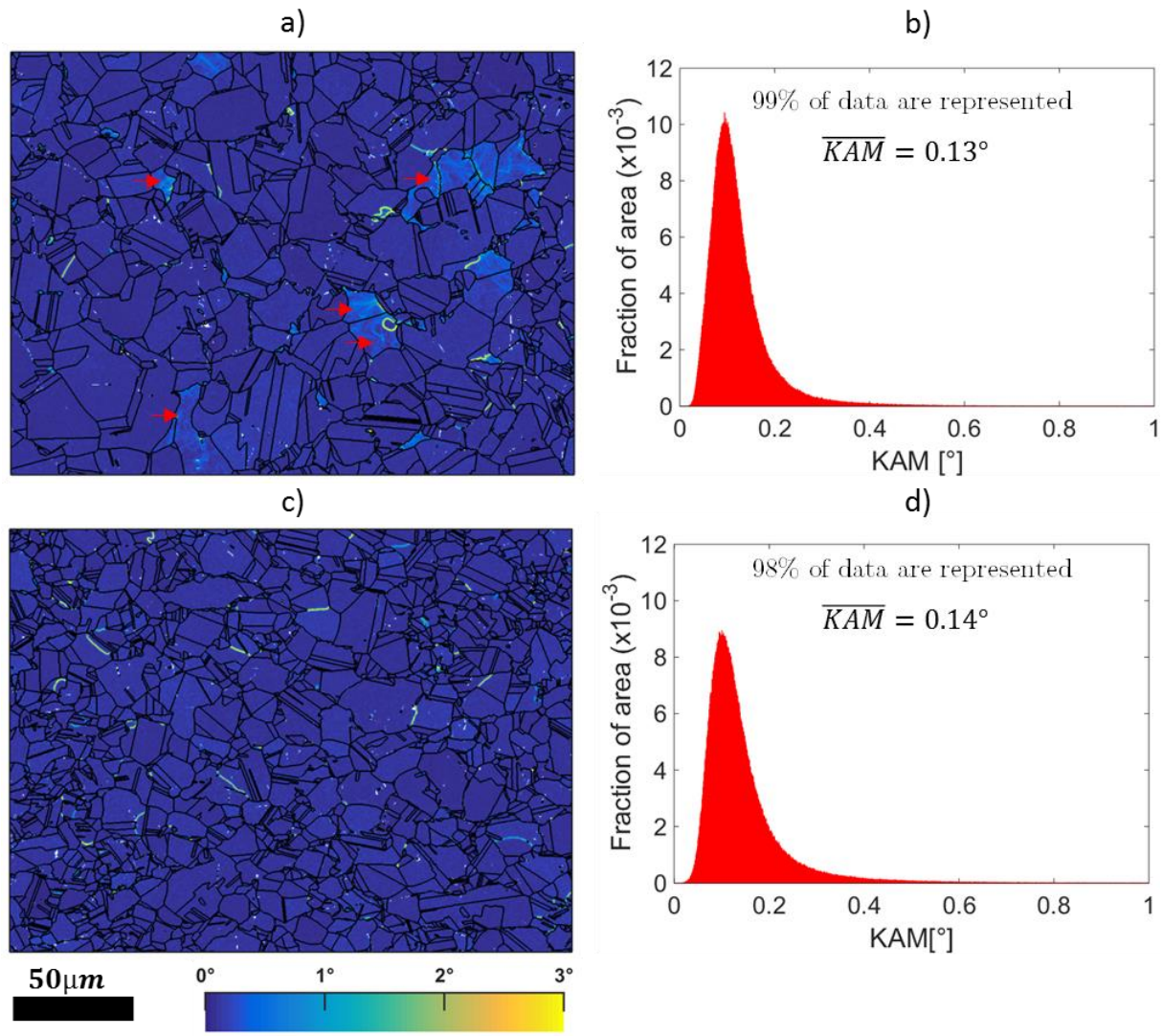

***Figure 5**: KAM maps(LLASS-filtered conventional EBSD data) and distributions of samples containing SRX grains used for ECCI in Figure4. a) and b) water quenched SRX grains, c) and d) slow cooled SRX grains. For the KAM distribution plots and average calculation, data coming from residual unrecrystallized grains (see red arrow on a) for example) and for grains constituted by less than 4 measuring points are not taken into account.*

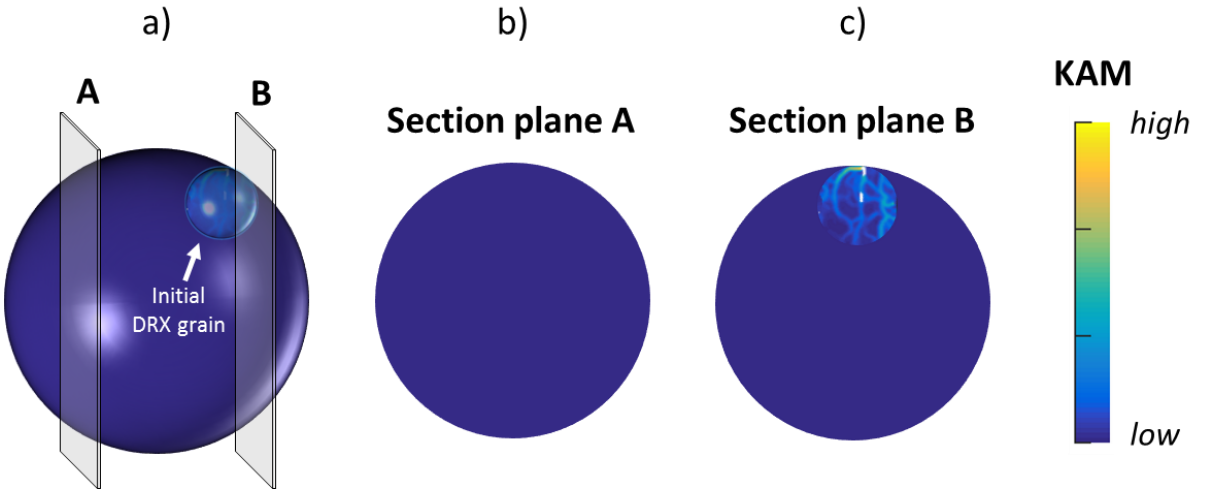

***Figure 6**: scheme explaining the difficulty of recognizing SRX and MDRX among PDRX grains in a 2D section. a) spherical 3D MDRX grain consisting in a spherical initial DRX grain (high KAM values, light blue) that has post-dynamically grown (the volume swept by the moving boundary has lower dislocation content, dark blue). b) and c) 2D sections of grain a), along*

the A and B planes, respectively. Section A does not meet the DRX initial grain, thus exhibits homogeneous low dislocation content and would be interpreted as a SRX grain. Section B comprises the initial DRX grain and can thus be recognized as a MDRX grain. The color coding refers to dislocation density or resulting KAM value.

2.2 DRX and PDRX populations: quantitative approach

Even if the KAM parameter is the most physical parameter for local dislocation density estimation via EBSD analyses, working with a single value per grain parameter such as GAKAM is more relevant to deal quantitatively with PDRX and DRX recrystallized fractions. Since KAM maps with improved angular resolution revealed the existence of DRX and PDRX grains in the analysed area (**Figure 2**), GAKAM maps and the corresponding GAKAM value distributions of the EBSD data already shown in **Figure 2** are plotted in **Figure 7,** with the same order as in **Figure 2**. Contrary to recrystallized/non-recrystallized grain discrimination, the coupling of GAKAM parameter with a grain size criterion is not relevant since DRX and PDRX grains have similar sizes. As a consequence, only the GAKAM parameter is taken into account in order to separate these populations quantitatively.

Once again, the progressive decrease in measurement noise reveals the two populations of recrystallized grains on **Figure 7**. The GAKAM map calculated from raw EBSD data acquired with standard angular resolution does not highlight a clear difference in GAKAM values for DRX and PDRX grains since some PDRX grains composed by noisy measurement points can have GAKAM values as high as some DRX grains. The corresponding distribution does not exhibit a clear threshold between both populations. Choosing a non-arbitrary threshold is difficult, resulting in a recrystallized grain classification that is far from being consistent with KAM maps at improved angular resolution.

On the contrary, the GAKAM map and distribution calculated from raw EBSD data acquired with the improved angular resolution methods highlight clearly the DRX and PDRX grain populations. The separation of these two recrystallized grain populations becomes obvious and is representative of the difference in dislocation density between DRX and PDRX grain populations seen on KAM maps. In consistence with observations done in section 2.1, filtering the raw data obtained with the improved angular resolution method using the LLASS filter still helps to define a GAKAM threshold for the separation of recrystallized grains populations. On the contrary, filtering the raw data obtained with the whole pattern indexing method does not change anything regarding the GAKAM threshold setting.

Even if the setting of threshold is not as obvious as for EBSD data acquired with improved angular resolution methods, filtering raw EBSD data acquired with standard angular resolution with LLASS filter, ever makes it possible to identify quantitatively DRX and PDRX grains reliably. Obviously, it is clear that the thresholds chosen on **Figure 7** could be set in a certain range of GAKAM values. In practice, for precise estimation of recrystallized grains populations, a first threshold can subsequently be refined based on the KAM map but this is out of the scope of the present paper which aims simply at demonstrating the possibility of separating DRX and PDRX grains populations when working with better angular resolved EBSD data. Within the area used for that demonstration, the DRX and PDRX area fractions could then be determined to be 50%-50% within a +/- 5% range.

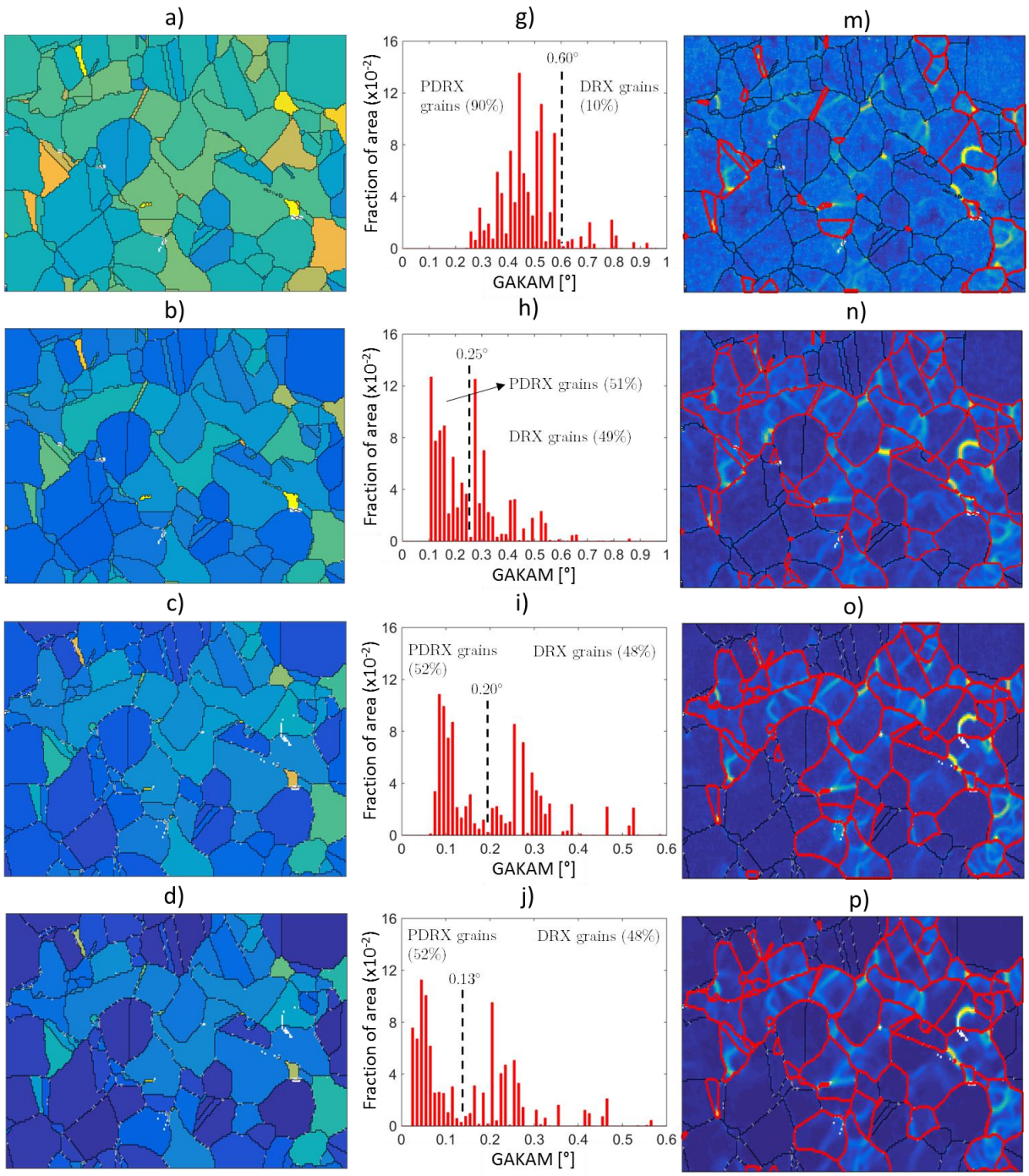
a)
g)
m)
b)
h)
n)
c)
i)
o)
d)
j)
p)
Fraction of area (x10-2)
GAKAM [°]
0.60°
PDRX grains (90%)
DRX grains (10%)
0.25°
PDRX grains (51%)
DRX grains (49%)
0.20°
PDRX grains (52%)
DRX grains (48%)
0.13°
PDRX grains (52%)
DRX grains (48%)

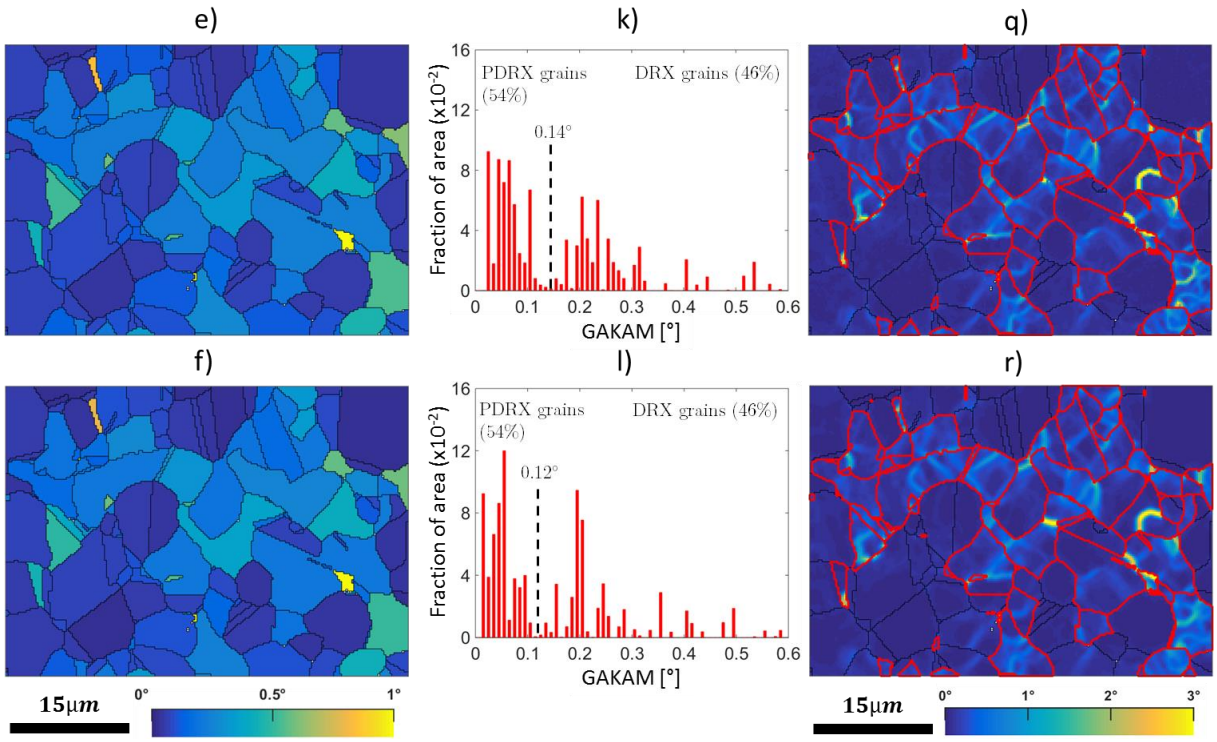

***Figure 7**: DRX and PDRX populations separation attempt. The first, third and fifth lines correspond respectively to raw EBSD data acquired with standard angular resolution and to raw EBSD data acquired with the improved angular resolution methods and the whole pattern indexing method. The second, fourth and sixth lines correspond respectively to the same data than first, third and fifth lines but post-processed with denoising LLASS filter. a)-f) GAKAM maps g)-l) GAKAM distributions with the set threshold and the corresponding estimation of DRX and PDRX proportions m)-r) the selected grains for DRX (surrounded in red) and PDRX populations are shown on KAM maps after a GAKAM thresholding.*

As shown previously, to enable the distinction between DRX and PDRX grains based on an objective GAKAM threshold value, limiting the noise level is required. Thus, an order of magnitude of noise level specific to each method has been assessed in order to estimate an approximate value for this limit. With any of the six presented methods, KAM distributions on the right column of **Figure 2** cannot be used to quantify precisely the orientation noise since some strain hardened regions (DRX grains) are present in the analysed area which lead to real higher local misorientations. As a consequence, in order to quantitatively assess the measurement noise inherent to each method more precisely, GAKAM values obtained by each method are reported in **Table 2** for four grains free of strain hardening identified on **Figure 2f**. Although the measurement noise is significantly impacted by the crystallographic orientation of the grain in standard angular resolution EBSD data, the orientation noise for the five other methods seems much less dependent on crystallographic orientation. The standard measurement noise previously estimated around 0.4° from **Figure 2g** is confirmed here with those single crystal values, it actually varies between 0.3 and 0.5° for the four selected grains. The three last methods listed in **Table 2** lead to similar orientation noise of approximately 0.05°, corresponding to the lowest measurement noise of the six presented methods. It can then be noted that the ultimate angular resolution reached after filtering raw conventional EBSD data with the LLASS filter is below 0.2° in the actual analysis conditions. Thus, reducing the noise measurement below 0.2° allows here the distinction between DRX and PDRX grains based on an objective GAKAM threshold value.

Grain (identified on **Figure 2f**)	a	b	c	d
Standard angular resolution – Raw data	0.53°	0.36°	0.39°	0.41°
Standard angular resolution – LLASS-filtered data	0.16°	0.13°	0.15°	0.17°
Improved angular resolution method – Raw data	0.09°	0.10°	0.12°	0.11°
Improved angular resolution method – LLASS-filtered data	0.04°	0.04°	0.06°	0.06°
Whole pattern indexing method – Raw data	0.04°	0.05°	0.05°	0.07°
Whole pattern indexing method – LLASS-filtered data	0.03°	0.04°	0.04°	0.06°

*Table 2: GAKAM values resulting from the different acquisition systems (raw data and LLASS-filtered data) for four grains free of strain hardening identified on **Figure 2f***

Conclusions

- Contrary to conventional EBSD analyses and the related standard angular resolution (in the range of 0.5°), improving the angular resolution allows for the discrimination of DRX and PDRX grains in EBSD maps via intragranular misorientation parameters.
- PDRX grains have indeed lower intragranular misorientation and dislocation densities as compared to DRX grains, as confirmed also by electron channeling contrast images.
- When water-quenched, PDRX grains exhibit some dislocations that are induced by thermal stresses upon fast cooling, but no measurable internal misorientations (even with enhanced angular resolution EBSD data).
- Indexing EBSD data using kinematic or dynamic pattern simulations (leading respectively to $\overline{KAM} = 0.22°$ and $\overline{KAM} = 0.17°$) improved substantially the angular resolution of the EBSD data as compared to the raw data ($\overline{KAM} = 0.50°$). Note that mean KAM values associated to each method must be taken as a means of comparing the measurement noise between each method. In no case these values must be considered as measurement precision since this feature depends on the sample used.
- Dynamic simulations provide enhanced angular resolution as compared to kinematic simulations.
- The LLASS filter is shown to be efficient enough in decreasing the orientation noise to allow for discriminating between DRX and PDRX grains, even starting from standard angular resolution EBSD dataset. It improves also the angular resolution of orientation maps refined using kinematic pattern simulations, but has no effect on data refined using dynamic pattern simulations.
- Discriminating MDRX and SRX among PDRX grains remains difficult based on 2D data, but the perspective of 3D EBSD analyses with low measurement noise should solve this issue.

Acknowledgment

The work received the financial support from the French Agency for Scientific Research (ANR) and from the Safran group via the industrial chair ANR-Safran OPALE. Pr Roland Logé (Thermomechanical Metallurgy Laboratory, EPFL) is acknowledged for allowing the access to a Gleeble machine with which the dynamically/post-dynamically recrystallized sample has been obtained. The authors are also very grateful to Dr Daniel Goran from the Bruker company (Berlin) who helped solving EBSD data format conversion issues and thus allowed adding Marc De Graef's method into the paper. And finally, M. De Graef would like to acknowledge financial support from an ONR Vannevar Bush Faculty Fellowship N00014-16-1-2821.

References

Azarbarmas, M., Aghaie-Khafri, M., Cabrera, J. M. & Calvo, J. (2016) Dynamic recrystallization mechanisms and twining evolution during hot deformation of Inconel 718. *Materials Science and Engineering A* **678**, 137-152.

Bachmann, F., Hielscher, R. & Schaeben, H. (2011) Grain detection from 2D and 3D EBSD data—Specification of the MTEX algorithm. *Ultramicroscopy*, **111**, 1720-1733.

Calcagnotto, M., Ponge, D., Demir, E. & Raabe, D. (2010) Orientation gradients and geometrically necessary dislocations in ultrafine grained dual-phase steels studied by 2D and 3D EBSD. *Materials Science and Engineering: A* **527**, 2738-2746.

Callahan, P.G. & M. De Graef (2013) Dynamical EBSD Patterns Part I: Pattern Simulations. *Microscopy and Microanalysis*, **19**, 1255-1265.

Chen, Y.H., Park S.U., Wei, D., Newstadt, G., Jackson, M., Simmons, J.P., De Graef, M. & Hero, A.O (2015) A dictionary approach to the EBSD indexing problem. *Microscopy and Microanalysis* **21**. 739-752.

Crimp, M.A., Simkin, B.A. & Ng, B.C. (2001) Demonstration of the g· bxu= 0 edge dislocation invisibility criterion for electron channelling contrast imaging. *Philosophical magazine letters*, **81**, 833-837.

Crimp, M. A. (2006) Scanning electron microscopy imaging of dislocations in bulk materials, using electron channeling contrast. *Microscopy research and technique* **69**, 374-381.

Hirsch, P. B., Howie, A., Nicholson, R. B., Pashley, D. W., & Whelan, M. J. (1966) *Electron microscopy of thin crystals*. 549 P. Butterworth Inc., Washington D.C.

Humphreys, F.J. & Hatherly, M. (2012). *Recrystallization and related annealing phenomena*. Elsevier.

Maitland, T., & Sitzman, S. (2007) *Electron backscatter diffraction (EBSD) technique and materials characterization examples.* Springer, Berlin.

Mansour, H., Guyon, J., Crimp, M.A., Gey, N., Beausir, B. & Maloufi, A.N. (2014) Accurate electron channeling contrast analysis of dislocations in fine grained bulk materials. *Scripta Materialia* **84**, 11-14.

Mansour, H., Goulden, J., Trimby, P., Bewick, A. (2017) Symmetry CMOS – New Detector Technology for EBSD. *Journées Annuelles SF2M 2017*.

Moussa, C., Bernacki, M., Besnard, R. & Bozzolo, N. (2015) About quantitative EBSD analysis of deformation and recovery substructures in pure Tantalum. In *IOP Conference Series: Materials Science and Engineering* **89**, 012038.

Na, Y.S., Yeom, J.T., Park, N.K. & Lee, J.Y. (2003) Simulation of microstructures for Alloy 718 blade forging using 3D FEM simulator. *Journal of Materials Processing Technology **141***, 337-342.

Poelt, P., Sommitsch, C., Mitsche, S. & Walter, M. (2006) Dynamic recrystallization of Ni-base alloys—Experimental results and comparisons with simulations. *Materials Science and Engineering: A* **420**, 306-314.

Powell, M. (2009) The BOBYQA Algorithm for Bound Constrained Optimization Without Derivatives. *Technical Report*, Department of Applied Mathematics and Theoretical Physics, Cambridge University, UK.

Sakai, T., Belyakov, A., Kaibyshev, R., Miura, H. & Jonas, J.J. (2014) Dynamic and post-dynamic recrystallization under hot, cold and severe plastic deformation conditions. *Progress in Materials Science* **60**, 130-207.

Schulson, E. M. (1977) Electron channelling patterns in scanning electron microscopy. *Journal of Materials Science* **12**, 1071-1087.

Seret, A., Moussa, C., Bernacki, M., Signorelli, R. & Bozzolo, N. Estimation of GND density from filtered EBSD data by automatic local linear calibration of smoothing splines, under revision for publication in *Journal of Applied Crystallography.*

Singh, S. & De Graef, M. (2016) Orientation sampling for dictionary-based diffraction pattern indexing methods. *Modelling and Simulation in Materials Science and Engineering* **24**, 085013.

Texier, D., Gómez, A.C., Pierret, S., Franchet, J.M., Pollock, T.M., Villechaise, P. & Cormier, J. (2016). Microstructural features controlling the variability in low-cycle fatigue properties of alloy Inconel 718DA at intermediate temperature. *Metallurgical and Materials Transactions A* **47**, 1096-1109.

Wang, Y., Shao, W.Z., Zhen, L., Yang, L. & Zhang, X.M. (2008) Flow behavior and microstructures of superalloy 718 during high temperature deformation. *Materials Science and Engineering: A* **497**, 479-486.

Zaefferer, S. & Elhami, N.N. (2014) Theory and application of electron channelling contrast imaging under controlled diffraction conditions. *Acta Materialia* **75**, 20-50.

Zhao, D. & Chaudhury, P.K. (1994). Effect of starting grain size on as-deformed microstructure in high temperature deformation of alloy 718. *Superalloys 718*, 625-706.

Zouari, M., Bozzolo, N. & Loge, R.E. (2016) Mean field modelling of dynamic and post-dynamic recrystallization during hot deformation of Inconel 718 in the absence of δ phase particles. *Materials Science and Engineering: A* **655**, 408-424.

Zouari, M., Logé, R.E. & Bozzolo, N. (2017) In Situ Characterization of Inconel 718 Post-Dynamic Recrystallization within a Scanning Electron Microscope. *Metals* **7**, 476.